

Three-dimensional nanofibrous sponges with controlled hierarchy regulating neural stem cell fate for spinal cord regeneration

Shilei Ni (✉ nishilei@sdu.edu.cn)

Qilu Hospital of Shandong University and Institute of Brain and Brain-Inspired Science, Cheeloo College of Medicine, Shandong University

Zhiwei Li

Qilu Hospital of Shandong University and Institute of Brain and Brain-Inspired Science, Cheeloo College of Medicine, Shandong University

Ye Qi

College of Textiles & Clothing, Qingdao University

Lei Sun

Qilu Hospital of Shandong University and Institute of Endocrine and Metabolic Diseases of Shandong University

Zheng Li

Qilu Hospital of Shandong University and Institute of Brain and Brain-Inspired Science, Cheeloo College of Medicine, Shandong University

Shaojun Chen

College of Textiles & Clothing, Qingdao University

Yuqi Zhang

Qilu Hospital of Shandong University and Institute of Brain and Brain-Inspired Science, Cheeloo College of Medicine, Shandong University

Yuan Ma

Qilu Hospital of Shandong University and Institute of Brain and Brain-Inspired Science, Cheeloo College of Medicine, Shandong University

Jinming Han

Qilu Hospital of Shandong University and Institute of Brain and Brain-Inspired Science, Cheeloo College of Medicine, Shandong University

Yulin Zhang

Qilu Hospital of Shandong University and Institute of Brain and Brain-Inspired Science, Cheeloo College of Medicine, Shandong University

Huimin Geng

Qilu Hospital of Shandong University and Institute of Brain and Brain-Inspired Science, Cheeloo College of Medicine, Shandong University

Bin Huang

Qilu hospital

Jian Wang

1. Qilu Hospital of Shandong University and Brain Science Research Institute, Shandong University 2.
Department of Biomedicine, University of Bergen, Jonas Lies vei 91, 5009-Bergen, Norway

<https://orcid.org/0000-0002-9482-5227>

Gang Li

Department of Neurosurgery, Qilu Hospital of Shandong University, Shandong University

Xingang Li

Shandong University <https://orcid.org/0000-0002-0878-0211>

Shaohua Wu

College of Textiles & Clothing, Qingdao University

Article

Keywords:

Posted Date: March 31st, 2022

DOI: <https://doi.org/10.21203/rs.3.rs-1491678/v1>

License: © ⓘ This work is licensed under a Creative Commons Attribution 4.0 International License.

[Read Full License](#)

Three-dimensional nanofibrous sponges with controlled hierarchy regulating neural stem cell fate for spinal cord regeneration

Abstract

A strategy combining biomimetic nanomaterial scaffolds with neural stem cell (NSC) transplantation holds promise for spinal cord injury (SCI) treatment. In this study, innovative three-dimensional (3D) nanofibrous sponges (NSs) are designed and developed by a combination of directional electrospinning and subsequent gas-foaming treatment. The as-generated 3D NSs exhibit uniaxially aligned nano-architecture and a highly controllable hierarchical structure with high porosity, outstanding hydrophilicity, and reasonable mechanical performance, and they are demonstrated to facilitate cell infiltration, induce cell alignment, promote neuronal differentiation of NSCs, and enhance their maturation by activating the cellular adhesion molecule (CAM) pathways. The *in vivo* data show that NSC-seeded 3D NSs efficiently promote axon reinnervation and remyelination in a rat model of SCI, with new “neural relays” constructed across the lesion gap. The recovery of coordinated locomotion and sensory function was both significantly improved, accompanied by the restoration of ascending and descending electrophysiological signalling. Overall, the present study indicates that the as-fabricated 3D NSs can effectively regulate the fate of NSCs, and an advanced combination of 3D NS

design and transplanted NSCs invites applications as an ideal tissue-engineered scaffold for SCI repair.

Introduction

Over 500,000 patients worldwide suffer permanent deficits in sensory and motor function due to spinal cord injury (SCI), resulting in tremendous socio-economic burdens¹. Unfortunately, no effective clinical treatment is yet available to repair the damaged spinal cord, mainly because the inhibitory and non-permissive microenvironment of SCI severely obstructs neuroregeneration and neural network reconnection^{2,3}. Most recently, neural tissue engineering (NTE) has emerged as a promising alternative for SCI repair, which can provide an instructive microenvironment to bridge the lesion gap of ascending and descending spinal tracts and support axon regeneration and functional recovery^{4,5}.

As a key aspect of NTE, biomaterial scaffolds are expected to largely resemble the native extracellular matrix (ECM) and thus effectively promote the regeneration and repair of damaged neural tissues⁶. In the past two decades, the design and construction of biomimetic nanomaterial scaffolds with high specific surface area, high porosity, and nano-architecture mimicking native ECM fibrils have attracted a great deal of attention in the field of NTE. Although there are numerous strategies, including phase separation, self-assembly, and

super-drawing, for the generation of nanomaterial-based scaffolds, electrospinning is a more promising approach to manufacture nanofibrous scaffolds, originating from its simplicity, versatility, and low cost⁷. The physical cues provided by electrospun nanofibres have been extensively demonstrated to improve cell-scaffold interactions, ECM deposition and remodelling and even guide stem cell differentiation⁸⁻¹⁰. Noticeably, compared with chaotically oriented nanofibre scaffolds, nanofibre scaffolds with aligned structures exhibited some obvious merits for SCI repair, which were demonstrated to effectively regulate the adhesion, elongation, orientation, and migration of neurons and glial cells, as well as effectively guide the directional regrowth and regeneration of axons at the SCI lesion site through the restoration of ascending and descending neural pathways and physiological function^{11,12}. Unfortunately, most electrospun nanofibres were collected in the form of mat-like structures with a two-dimensional (2D) dense structure and small pore size, inevitably resulting in low cell infiltration and unsatisfactory regeneration outcomes for 3D neural tissues^{13,14}. It still remains a tremendous technical challenge to design and develop a novel electrospinning-based biomaterial scaffold integrated with a uniaxially aligned structure and 3D ECM-mimicking hierarchical structure while maintaining the desirable nanofibrous characteristics and appropriate physicochemical properties.

Cells are also of significant importance for NTE applications¹⁵. Neural stem

cells (NSCs) are a class of cells with self-renewal ability and multilineage differentiation potential. In response to SCI, a few endogenous NSCs can be quickly activated and differentiated into different cell types¹⁶. However, due to the harsh microenvironment of SCI, most activated NSCs differentiate into astrocytes rather than neuronal lineage cells, making it difficult for them to take on neurological functions^{17,18}. The implantation of exogenous propagated NSCs seems to be a promising strategy for SCI repair¹⁰. However, owing to the lack of a support system, direct injection of NSCs into the lesion cavity does not achieve satisfactory results¹⁹. Worse still, previous studies have indicated that NSCs also mostly differentiate into astrocytes if the cells are loaded in an inappropriate scaffold structure¹⁹. Therefore, constructing an ideal cell scaffold that can effectively regulate and control the fate of NSCs remains an intractable challenge for SCI treatment.

To overcome the above challenges, our present study first designed and implemented novel 3D gas-foaming nanofibrous sponges (NSs) with aligned structures and controlled hierarchies to guide the neural differentiation of NSCs. Then, exogenous NSCs harvested from foetal rats were seeded on the as-prepared 3D NSs and were further implanted into the lesion gap to bridge nerve stumps in a spinal cord hemisection rat model of SCI. Specifically, an integrated strategy combining directional electrospinning with gas-foaming technology was utilized to generate 3D NSs through gas bubble expansion

between the adjacent nanofibre layers of electrospun 2D polycaprolactone (PCL)/poly(p-dioxanone) (PPDO) mats. The as-generated 3D NSs were expected to possess a laminated structure with ECM-mimicking aligned nanotopography, a controllable hierarchical structure, high porosity and hydrophilicity, thereby providing an instructive microenvironment to induce the regeneration of the damaged spinal cord. The internal spacing between the layers of 3D NSs was designed at the microscale, which was expected to provide optimal widths for NSC infiltration and proliferation. Meanwhile, the aligned nanofibrous structure maintained in each layer was expected to guide the migration and alignment of both grafted and host neural cells. Except for a series of *in vitro* studies, SCI rats were utilized to verify the regenerative effects by employing our NSC-loaded 3D NSs for SCI treatment. A schematic illustration of the whole study is shown in Figure 1.

Results

1. Fabrication and characterization of 3D NSs.

A directional electrospinning method was first utilized to fabricate 2D PCL/PPDO nanofibrous mats (NMs) (Figure 2A(a1)), which were subsequently transformed into 3D PCL/PPDO NSs (Figure 2A(a2)) through the expansion of gas bubbles generated in an aqueous solution of NaBH₄. SEM images (Figure 2A(a1)) showed that the as-fabricated 2D PCL/PPDO NMs exhibited a uniaxially aligned nanofibrous structure, and the fibres presented a bead-free

and smooth morphology with a mean fibre diameter of 394.7 ± 99.3 nm. A typical gas-foaming process is shown in Supplementary Video S1. SEM images (Figure 2A(a2)) showed that the as-expanded PCL/PPDO NSs possessed a 3D laminated structure with a controllable hierarchical structure while maintaining the uniaxially aligned nanofibrous morphology originating from the 2D PCL/PPDO NMs, indicating that the hydrogen bubbles in the expansion process separated the nanofibres into different layers, but the necessary connections still existed between adjacent layers. With increasing time of the gas-foaming process, a series of 3D NSs with different expansion heights could be generated (Figure 2B). The initial 2D NMs displayed a dense sheet-like structure with a thickness of 0.13 ± 0.01 mm. By comparison, the thickness of the 3D NSs increased to 2.3 ± 0.67 mm, 3.8 ± 0.79 mm, 5.4 ± 1.1 mm, and 8.9 ± 1.2 mm when the gas-foaming time was set as 10 min, 20 min, 40 min, and 60 min in the 0.04 M NaBH₄ solution (Figure 2B, and Supplementary Figure S1). More importantly, the porosity of 3D NSs presented an upwards trend with increasing gas foaming time when the dense 2D structure was expanded into a porous 3D structure. Specifically, the porosity of the 3D NSs rapidly increased in the first 10 min of expansion (from $75.46 \pm 3.21\%$ (2D NMs) to $90.35 \pm 3.73\%$) and then gradually remained constant ($94.86 \pm 1.61\%$ at 20 min, $97.02 \pm 0.39\%$ at 40 min, and $98.14 \pm 0.36\%$ at 60 min) (Figure 2C).

The hydrophilicity and wettability of engineered scaffolds play a critical role in cell-scaffold interactions in NTE. The combination of hydrophilic biomaterials and gas-foaming technology was carried out to improve the surface hydrophilicity of electrospun scaffolds. The water contact angles of hydrophobic electrospun 2D PCL NMs changed from the initial 128.7° to 116.3° after 90 s (Supplementary Figure S2), while hydrophilic electrospun 2D PPDO NMs were able to absorb a droplet quickly (within 4 s). After mixing PCL and PPDO into one electrospinning system, the contact angle of 2D PCL/PPDO NMs was greatly improved from the initial 102.1° to 21.6° after 90 s. Interestingly, a dramatically improved surface hydrophilicity was found for the 3D porous PCL/PPDO NSs generated from the gas-foaming strategy, which could absorb a droplet immediately (in less than 1 s; Figure 2D and Supplementary Video S2). It was also found that the gas foaming time had positive effects on the water absorption capacity of 3D PCL/PPDO NSs, which were $18.02 \pm 3.36\%$, $22.47 \pm 2.43\%$, $31.19 \pm 2.94\%$, and $37.83 \pm 1.21\%$ after 10, 20, 40, and 60 min of expansion, respectively (Figure 2E). In comparison, the water absorption was only $9.13 \pm 1.12\%$ for the original unexpanded 2D PCL/PPDO mats. The increased surface hydrophilicity and water absorption of 3D PCL/PPDO NSs were attributed to the significantly increased porosity after gas-foaming expansion. We also demonstrated that the NaBH_4 concentration positively influenced the expansion height, porosity, and water absorption ability of the 3D NSs that were ultimately generated, and the corresponding

data are presented in Supplementary Figure S3.

The FTIR spectra were utilized to determine the alteration of chemical groups of 2D PCL NMs, 2D PPDO NMs, 2D PCL/PPDO NMs, and 3D PCL/PPDO NSs (Figure 2F). The data clearly showed that the positions of the characteristic peaks had no obvious shifting after spinning a blend of PCL and PPDO, indicating that no new chemical groups were generated during blend electrospinning. The absorption peaks centred at 2945 cm^{-1} and 2868 cm^{-1} were attributed to the stretching vibration of C-H. The peaks at 1724 cm^{-1} and 1472 cm^{-1} were assigned to the stretching vibration of C=O and the bending vibration of CH_2 , respectively. In addition, the three peaks at 1234 cm^{-1} , 1168 cm^{-1} , and 1042 cm^{-1} all belonged to the stretching vibration of C-O. It was also found that no chemical reaction occurred during the gas-forming process. X-ray diffraction (XRD) analysis was performed to determine the crystallinity of the abovementioned nanofibre samples (Figure 2G). All four samples exhibited two sets of obvious diffraction peaks located at approximately 21.3° and 23.6° , which were assigned to the (110) and (200) crystal planes, respectively. Importantly, the 3D PCL/PPDO NSs exhibited significantly increased diffraction peak intensity compared with other 2D NM groups, indicating that the gas-foaming technology could effectively improve the crystallinity of nanofibre scaffolds.

The results from the tensile test showed that both 2D PCL/PPDO NMs and 3D PCL/PPDO NSs exhibited similar tensile load-elongation curves (Figure 2H(h1)). The Young's modulus of 3D PCL/PPDO NSs was found to be significantly lower than those of 2D PCL/PPDO NMs (0.61 ± 0.12 MPa vs. 89.34 ± 5.09 MPa) (Figure 2H(h2)); thus, the Young's modulus of 3D NSs was close to that of the normal spinal cord (200–600 kPa)². Moreover, the 3D PCL/PPDO NSs showed notably lower breaking stress but obviously higher breaking strain than the 2D PCL/PPDO NMs (Figure 2H(h2 and 3)). Supplementary Video S3 shows that our 3D PCL/PPDO NSs could reassume their shape under the action of repeated compression forces. The excellent elastic recovery properties were beneficial for maintaining the stability of the porous structure during *in vivo* transplantation.

2. 3D NSs enhanced the survival, neuronal differentiation, and maturation of NSCs.

Biocompatibility is the primary factor for an ideal transplantable biomaterial scaffold, and NSCs were seeded and cultured on 3D PCL/PPDO NSs to investigate the cell-scaffold interaction (Figure 3A). Classical and widely used 2D tissue culture polystyrene (TCPS) plates were also employed to culture NSCs as a control. The images from live/dead staining (Figure 3B and Supplementary Figure S4) showed that the NSCs seeded on 3D NSs presented a high survival rate (approximately 90%) throughout 7 days of

culture, which was similar to those cultured on 2D TCPS control plates control. A low-magnification view of live/dead staining (Figure 3B) also demonstrated that a hierarchical arrangement of NSCs was formed after 7 days of culture, which exhibited great orientation and neural connections between adjacent layers in the 3D NSs. The results from Cell Counting Kit-8 (CCK-8) assays showed that the NSCs exhibited vigorous cell viability when seeded on 3D NSs (Figure 3C).

Immunofluorescence (IF) staining was further employed to evaluate the stemness of NSCs after 1 and 7 days of culture (Figure 3D-F). The percentage of Nestin⁺ cells cultured on 3D NSs was significantly less than that in the control group ($52.37 \pm 12.35\%$ vs. $85.94 \pm 8.68\%$, $P < 0.01$) at day 1. In addition, the expression of neural-specific markers, including β III tubulin (Tuj-1), glial fibrillary acid protein (GFAP), neurofilament 200 (NF200), doublecortin (DCX), and Synapsin-1 (Syn), was assessed to explore the differentiation direction of NSCs at day 7. GFAP is mainly distributed in astrocytes, while Tuj-1 is a specific marker of early neurons reflecting neurite outgrowth. Figure 3G and 3H show that 3D NSs could significantly promote NSC differentiation towards neurons with lively outgrowing and uniaxially aligned axons along the nanofibre alignment. Semi-quantitative analysis of the fluorescent signal also revealed that the ratio of Tuj-1⁺ cells in the 3D NSs was approximately 14 times higher than that in the 2D control (Figure 3I), while the ratio of GFAP⁺

cells in the 3D NS group was approximately half of that in the 2D control (Figure 3J). It is well known that synaptic signal transduction between neurons is the basis of neural function. Therefore, it is extraordinarily important to further explore the synapse level in 3D NSs. Syn is an abundant neural protein for regulating neurotransmitter release and primarily serves as a coating protein on synaptic vesicles. Through IF staining of Syn and NF200, Figure 3K illustrates that complex neural synaptic networks were constructed in the 3D NS group, with a large number of neural axons, tight intercellular connections, and intensive synaptic vesicles being observed. IF staining of DCX (mainly expressed in neuroblasts and immature neurons) and NF200 also demonstrated strong axon regeneration and neurogenesis of NSCs in the 3D NS group (Figure 3L). Additionally, the morphology of NSCs in the 3D NSs is presented in Figure 3M. This clearly indicated that NSCs were arranged along the longitudinally oriented nanofibres and axons intercommunicated to form neural networks.

Real-time quantitative polymerase chain reaction (RT-qPCR) was also performed to assess the expression of neural-specific gene markers after 7 days of culture. The relative expression of *Tuj-1*, *Gfap*, and oligodendrocyte transcription factor 2 (*Olig2*) mRNA in the 3D NS group significantly increased by 38.9-, 1.4-, and 4.2-fold compared to the 2D control, respectively. This finding implied that the ECM-mimicking topography of 3D NSs had positive

impacts on the induction of neuronal lineage of NSCs, which reinforced the above statement about IF staining. To further explore the potential molecular mechanisms of neural differentiation, several representative neural differentiation-related genes, including neuronal differentiation 1 (*NeuroD1*), mammalian achaete-scute homologue-1 (*Mash1*), Hes family basic helix–loop–helix transcription factor 6 (*Hes6*), Wnt family member 7a (*Wnt7a*), and neurogenin 2 (*Ngn2*), were further determined through RT–qPCR. Figure 3Q clearly shows that the mRNA levels of all the above-mentioned genes were significantly increased in the 3D NS group, increasing 5.7-fold for *NeuroD1*, 1.7-fold for *Mash1*, 1.4-fold for *Hes6*, 30.6-fold for *Wnt7a*, and 17.2-fold for *Ngn2* compared to those in the 2D control. In contrast, some typical stemness-related genes, e.g., *Nestin*, nuclear receptor subfamily 2 group E member 1 (*NR2E1*), and Hes family basic helix–loop–helix transcription factor 5 (*Hes5*), were found to be downregulated in the 3D NS group (Figure 3R). Taken together, it can be concluded that the as-developed 3D NSs with uniaxially aligned nanofibrous structures and a 3D ECM-mimicking hierarchical structure and mechanics could enhance the survival, neuronal differentiation, and maturation of NSCs.

3. Transplantation of exogenous NSC-loaded 3D NSs enhanced neurological functional recovery in rat SCI models.

The *in vivo* performance of 3D NSs was comprehensively evaluated by using

the T10 spinal cord hemi-section model in SD rats (Supplementary Figure S5), and the timeline and characterization methods are shown in Figure 4A. The walking patterns of SCI rats are recorded in Supplementary Video S4, revealing that the combination of 3D NSs and NSCs significantly improved locomotor function and coordination. The sensory testing results revealed that the animals in the 3D NS + NSC group exhibited a faster response (44.3 ± 16.9 s) than the SCI group (134.6 ± 42.3 s) and the 3D NS group (60.5 ± 30.1 s) (Figure 4B). The results based on Basso, Beattie, and Bresnahan (BBB) locomotor scores showed that no hindlimb movement was observed in SCI rats with a BBB score of 0 on day 14. As expected, the 3D NS + NSC group showed enhanced recovery compared with the SCI and 3D NS groups from 1 week post-injury (wpi) and thereafter, with regaining locomotor coordination, which requires a minimum BBB score of 12. Similarly, the incline plane tests revealed that the 3D NS + NSC group ($62.2 \pm 2.4^\circ$, $65.2 \pm 5.1^\circ$, and $67.4 \pm 2.5^\circ$) exhibited stronger hindlimb grip and better body coordination than the SCI ($49.2 \pm 4.2^\circ$, $50.2 \pm 3.7^\circ$, and $52.1 \pm 2.5^\circ$) and 3D NS groups ($57.8 \pm 0.8^\circ$, $60.1 \pm 2.3^\circ$, and $61.4 \pm 1.6^\circ$) at 4, 6, and 8 wpi, respectively (Figure 4D). Footprint analysis was also utilized to test locomotor recovery at 8 wpi (Figure 4E). Following SCI, the coordination of the fore- and hindpaws was severely impaired, leading to the obvious dragging of hindlimbs and non-overlapping fore- and hindpaw footprints with an increase in rotation angle and relative position (the distance between the ipsilateral fore- and hindpaws). However,

287 3D NS transplantation significantly reduced the rotation angle (Figure 4F) and
288 relative position (Figure 4G) of the ipsilateral hindlimbs, suggesting good
289 recovery of interlimb coordination over that time frame. Importantly, the 3D NS
290 + NSC group still showed improved locomotor performance compared with the
291 3D NS group.

292
293 MR imaging (MRI) data with T2-weighted turbo spin-echo images (T2WI) were
294 collected to assess the gross recovery of transected spinal cords at 4 wpi
295 (Figure 4H). An obvious gap was still observed in the SCI group, indicating
296 almost no recovery with poor continuity if no treatment was taken after SCI. In
297 comparison, the implanted 3D NSs could enhance the migration and
298 penetration of cells, resulting in the partial restoration of the anatomical
299 structure of the transected spinal cord. Noticeably, the NSC-loaded 3D NS
300 group was found to exhibit the highest continuity compared with the SCI group
301 and 3D NS group.

302
303 The electrophysiological evaluation was carried out to test the
304 electrophysiological conductivity of regenerated spinal cords at 8 wpi. As
305 shown in Figure 4I and J, motor evoked potentials (MEPs) and somatosensory
306 evoked potentials (SEPs) were measured to monitor the descending and
307 ascending electrophysiological signals, respectively. Poor electrical conduction
308 with notably decreased amplitude and extended latency for both MEP and

SEP was present in the SCI group. In comparison, the 3D NS group and 3D NS + NSC group showed significantly enhanced electrophysiological recovery, with amplitude rising and latency dropping through the reconstruction of neural relays replacing the damaged spinal cord (Figure 4K-N).

4. Histological evaluation of the regenerated spinal cord.

Double IF staining of Tuj-1 and GFAP was employed at 8 wpi (Figure 5A-D) to assess the capability of 3D NSs to direct neuronal differentiation and maturation of exogenous and endogenous NSCs. In the SCI group, Tuj-1⁺ and GFAP⁺ cells were barely detectable (Figure 5B), while the 3D NS group showed a few Tuj-1⁺ neurons (areas of $1.3 \pm 1.1\%$) and sporadic GFAP⁺ astrocytes (areas of $4.3 \pm 1.2\%$) (Figure 5C). This result suggested that the aligned ECM-mimicking hierarchical structure provided specific guidance cues to enhance the recruitment of endogenous neural cells to the lesion site. As a control, the 3D NS + NSC group presented a significantly larger population of Tuj-1⁺ (areas of $12.7 \pm 5.1\%$) and GFAP⁺ (areas of $12.5 \pm 5.2\%$) cells (Figure 5D) than the other two groups (Figure 5I and J). To trace the fate of grafted NSCs and distinguish them from host neural cells, green fluorescence protein (GFP)-expressing NSCs were isolated from GFP⁺ embryonic rats and seeded on 3D NSs, which were further implanted into the lesion site of SCI rats (Supplementary Figure S6A-C). A number of cells positive for both GFP and NeuN (a marker of mature neurons) were present in the lesion site at 8 wpi

(Supplementary Figure S6D). The data demonstrated that pre-differentiated exogenous NSCs were capable of survival for a long time in the lesion site under the shield of 3D NSs. Furthermore, the 3D biomimetic scaffolds could guide cell growth and promote NSC differentiation and maturation towards the neurological lineage. More importantly, we found that the grafted NSCs were surrounded by host neurons, which might facilitate the integration of donor NSCs with host tissue.

We further checked whether the as-differentiated mature neurons could perform neural functions. IF staining of NF200/ChAT (cholinergic neuronal marker) and NF200/5-HT (serotonergic neuron marker) was carried out. A large population of ChAT⁺ ($8.1 \pm 2.7\%$) and 5-HT⁺ ($1.7 \pm 0.3\%$) cells was observed at the lesion site in the 3D NS + NSC group (Figure 5E and F), which reached 39% and 48% of the Sham group, respectively (Figure 5N, O and Supplementary Figure S7). Moreover, the 3D NSs guided axons to form close cell contacts where mature neurons were surrounded by a large number of VGlut2⁺ synapses (excitatory synaptic marker) (Supplementary Figure S9).

Next, a variety of histological staining methods, including Luxol fast blue (LFB) staining, Nissl staining, and H&E staining, were performed for further evaluation of histological recovery of regenerated spinal cords. LFB staining showed that the 3D NS + NSC group exhibited the highest myelin regeneration

capacity (Figure 5G-J), which supported axons to aid metabolism and integrity²⁰. There was no remyelination detectable in the SCI group, while the myelin areas of the 3D NS and 3D NS + NSC groups reached $23.3 \pm 3.1\%$ and $29.0 \pm 3.5\%$, respectively (Figure 5M). Nissl staining was used to assess the morphology and distribution of neurological cells in longitudinal sections (Figure 5P and Q) and cross-sections (Supplementary Figure S8A-C). A large number of neural cells penetrated the inner part of the scaffold with high porosity and a multi-layered structure. H&E staining images were consistent with the above histological results (Supplementary Figure S8D-G). A large gap was found at the lesion site in the SCI group, while the 3D sponge, as a bridge, could guide the growth and migration of cells. Finally, the gross view of the spinal cord revealed that only a few connective tissues were present at the lesion area of SCI rats, while the spinal cord with 3D NSs showed relatively intact anatomy (Supplementary Figure S8H). Taken together, these results indicated that the porous 3D NSs exhibit uniaxially aligned nano-architecture and a highly controllable hierarchical structure, which promoted cell survival, infiltration, differentiation, and maturation after SCI treatment.

In addition, it is worth noting that the recovery of spinal cord neurological function is generally accompanied by the restoration of corresponding muscle anatomical structure and biological function²¹. As shown in Supplementary Figure S10A, SCI rats exhibited apparent atrophy of the ipsilateral

gastrocnemius muscle in the gross view, while the 3D NS group and 3D NS + NSC group reversed this outcome. Masson trichrome staining indicated that the number of collagen fibres increased dramatically with a smaller diameter of muscle fibres in the SCI group than those in the Sham group (Supplementary Figure S10B-E). The transplantation of 3D NSs could significantly improve the histological performance of the ipsilateral gastrocnemius muscle. Specifically, the mean diameter of muscle fibres was determined to be $40.7 \pm 4.5 \mu\text{m}$, $10.0 \pm 1.4 \mu\text{m}$, $30.6 \pm 0.7 \mu\text{m}$, and $35.9 \pm 1.3 \mu\text{m}$ in the Sham, SCI, NS, and NS + NSC groups, respectively (Supplementary Figure S10F). Similarly, the 3D NS + NSC group had a significantly increased percentage of muscle fibre area (Supplementary Figure S10G). Then, the weight of wet muscle was analysed to further verify the atrophy degree (Supplementary Figure S10H). The gastrocnemius muscle in the 3D NS + NSC group was approximately 3.9-fold that in the SCI group. In summary, the gas-foaming scaffolds were effective for muscle anatomy and functional recovery.

5. Mechanism of enhanced neurogenesis from NSCs by the use of 3D NSs.

The abovementioned results clearly demonstrated that the 3D NSs could effectively regulate the neuronal differentiation of NSCs, so the molecular mechanism involved was investigated in this section. RNA sequencing was carried out to analyse differentially expressed genes (DEGs) of NSCs seeded

on the 3D NSs and 2D TCPS control plates after 7 days of culture (Supplementary Figure S11A). The volcano plot showed that the numbers of upregulated genes and downregulated genes were 499 and 396, respectively (Supplementary Figure S11B). Furthermore, gene ontology (GO) was analysed based on three ontologies: biological process (BP), cellular component (CC), and molecular function (MF) (Supplementary Figure S11D). Figure 6A and B display the gene-concept network and enrichment map of BP and reveal that the top 10 pathways mainly targeted cilium organization, axoneme assembly, and microtubule-based movement. The CC analysis implied a connection with the focused network formed in the axoneme and synapse (Figure 6C and D), which was highly consistent with the BP results. In addition, MF analysis indicated that NSCs on the 3D NSs were involved in cell–cell adhesion mediator activity, cell adhesion molecule (CAM) binding, and ATP-dependent microtubule motor activity (Supplementary Figure S11C). Furthermore, Kyoto Encyclopedia of Genes and Genomes (KEGG) enrichment was employed to better understand the involved complex signalling pathways using 3D NSs to culture NSCs. Figure 6E indicates that the MAPK signalling pathway, CAM, calcium signalling pathway, focal adhesion, and other neuro-enriched pathways were considered to be involved when the 3D NSs were utilized to regulate the fate NSCs.

Based on the above analysis, the potential mechanism by which 3D NSs

regulate NSC neurogenesis is proposed in Figure 6F. NSCs adhered to the ECM-mimicking nanofibres, resulting in the activation of CAM binding. The interaction between the CAM of NSCs and nanofibres was the initial factor for a series of downstream signalling pathways, including the MAPK pathways, which played crucial roles in the regulation of neuronal differentiation, axon regeneration, synaptic formation, and other important neurophysiological processes.

Discussion

The regeneration of neurons and axons throughout the injured site is critical to SCI repair. NTE offers a versatile and powerful platform for the construction of neural relays consisting of biomimetic nanomaterials and functional cells²². Although several advanced techniques have been developed to generate 3D electrospun scaffolds capable of enhancing cellular infiltration, they still have a few limitations that could be improved for NTE application²³. First, most of the previous 3D electrospun scaffolds were composed of randomly oriented nanofibres and uncontrolled porosity, which are not suitable for highly organized neural tissues^{12,24}. Although a few post-processing technologies, such as ultrasonication, might preserve the oriented topographic cues, the molecular weights of materials and mechanical properties of nanofibres would be significantly affected by insufficient thickness and uneven geometry⁶. Alternatively, other studies previously developed microfibre-based tissue

engineering scaffolds with much larger diameters. However, such large microfibres lack nanotopographic cues and ECM-mimicking properties, leading to low adhesion and growth of neural cells²⁵. Therefore, it is critical yet challenging to develop a simple, controllable, and uniform technology to fabricate 3D biomimetic scaffolds for neural regeneration.

In this study, we introduced novel 3D PCL/PPDO NSs through the combination of directional electrospinning and gas-foaming technology, which effectively overcame the above obstacles. Utilizing this approach, the imparted anisotropic cues of biomimetic scaffolds would be completely preserved, presenting uniaxially aligned nano-architecture and a highly controllable hierarchical structure (Figure 2A). We have demonstrated that such an ECM-mimicking hierarchical structure provides an excellent microenvironment to regulate the fate of loaded NSCs without any supplemental neurotrophins or additives (Figure 3). First, compared with dense 2D NMs, the porous nanostructure ($98.12 \pm 0.67\%$ porosity) of 3D NSs significantly enhances the penetration of attached cells, oxygen and nutrient exchange, and metabolite emission, which are the essential factors for maintaining cellular survival (Figure 3B, 2C, and Supplementary Figure S4). Additionally, previous studies indicated that approximately 200 μm diameter microchannel scaffolds were the most effective for linear axon guidance²⁶, while channels larger than 400 μm in diameter were not conducive to nerve regeneration²². Under the precise

control of the expanding process, the controlled hierarchical structure provides natural micro-channels with a 150~200 μm spacing, which is appropriate for the migration and communication of neural cells (Figure 2A and 3B). Third, the hydrophilicity of engineered scaffolds was another critical factor affecting cell-scaffold interactions. Surprisingly, the expansion process dramatically increases the surface hydrophilicity of 3D PCL/PPDO NSs, which can immediately absorb a droplet for less than 1 s (Figure 2D). Fourth, the elastic modulus of the 3D NSs significantly decreased from 89.34 ± 5.09 MPa to 0.61 ± 0.12 MPa (Figure 2F), highly similar to native spinal cords (200–600 kPa)^{27,28}. It is worth noting that the mismatch of scaffold stress will cause a severe inflammatory response at the implant-host interface and compression and laceration of the spinal cord²⁹. However, the 3D NSs, with their similarity to the native spinal cord, dramatically promoted differentiation towards neurons with an increasing *Tuj-1* mRNA expression (38.9-fold) and Tuj-1+ cell ratio (14-fold) (Figure 3I and N), which further induced NSC maturation with neurofilament growth and synaptic formation (Figure 3K). In summary, these results strongly indicated that 3D NSs with porous structures, outstanding hydrophilicity, and reasonable mechanical performance significantly promoted the survival, migration, differentiation, and maturation of NSCs *in vitro*.

However, it is difficult for NSC grafts to survive for a long time *in vivo* due to the deleterious microenvironment in lesion sites^{2,30}. The ECM-mimicking

hierarchical structure of the as-fabricated 3D NSs can provide a more suitable environment for cell survival, neuronal differentiation, and maturation. Strikingly, the GFP-labelled NSCs within the 3D NSs still survived in the lesion epicentre and differentiated into mature neurons (NeuN⁺) 8 weeks after transplantation (Supplementary Figure S6). Some endogenous cells also migrated along the longitudinally oriented scaffolds to the lesion site and differentiated into neurons (GFP⁻/NeuN⁺). Clearly, these results indicated that exogenous NSCs may secrete multiple neurotrophins to recruit endogenous neural cells engaging in SCI repair¹⁰. As expected, neurological function and anatomic structure were significantly improved in the hemisectioned SCI rat model. Overall, the as-fabricated 3D NSs provide important neuroprotection and guidance to the newly formed “neural relay”, allowing axon regeneration, myelinogenesis, and synaptic reconnections.

Furthermore, the potential mechanism of the neuronal response to anisotropic topographic features of 3D NSs was elucidated through mRNA sequencing (Figure 6). When NSCs attach to ECM-mimicking nanofibres, growth cones and focal adhesion are involved in cell behaviour regulation¹². Growth cones are the sensitive structure at the apical end of growing axons, which consist of microtubules and actin filaments. These microtubules and filaments enable the perception of morphology-associated cues through the formation of a complex interacting meshwork. Then, to minimize cell cytoskeleton distortion caused by

anisotropic cues, microtubules can grow and shrink dynamically to align with the directional nanofibrous structure³¹. In addition, it was confirmed that focal adhesion also played an important role in mediating neurite outgrowth along the biomimetic scaffolds, which was a complex protein cluster that integrates the cytoskeleton with the adhesion substrates through CAM activation³². Among them, integrin binding is an initial factor of downstream signal transduction with calcium signalling activation, causing gradual changes in cell morphology and biological functions^{32,33}. Therefore, we presume that growth cones and focal adhesion are the bridges between the ECM-mimicking cues of 3D NSs and neural cell behaviours by activating the CAM-based MAPK/PI3K-AKT signalling cascade.

Method

Fabrication of 2D PCL/PPDO NMs.

PCL (Mw = 80,000, Sigma Aldrich, USA) and PPDO (Mw = 100,000, Corbion Purac, Netherlands) with a mass ratio of 4:1 were dissolved in hexafluoro-2-propanol (HFIP, purity ≥ 99.8%, Aladdin Reagent, China) to generate a homogeneous spinning solution with a total concentration of 10% (w/v). A directional electrospinning device employing a rotating cylinder as a nanofibre collector was utilized to spin the PCL/PPDO solution into uniaxially aligned nanofibres (Figure 1). The applied voltage, spinning distance, and solution feeding rate were set at 12 kV, 16 cm, and 0.8 mL/h, respectively. The

rotating speed of the cylinder collector was fixed at 1700 r/min.

Fabrication of 3D NSs through a gas-foaming strategy.

The 2D PCL/PPDO NMs were expanded into 3D NSs by gas foaming technology. The pre-cut 2D NMs were immersed into NaBH₄ (Sinopharm Chemical Reagent Co., LTD., China) aqueous solution with different concentrations (1 M, 2 M, 3 M, 4 M). The hydrogen bubbles could be continuously generated through the chemical reaction $\text{NaBH}_4 + 2\text{H}_2\text{O} \rightarrow \text{NaBO}_2 + 4\text{H}_2\uparrow$. The as-formed hydrogen bubbles penetrated the 2D NMs and expanded the 2D NMs into 3D NSs. Supplementary Video S1 presents a typical gas-foaming process. After the predetermined time point, the as-expanded 2D NMs were removed and further washed 5 times to remove the residual NaBH₄. The final harvested 3D NSs were lyophilized and stored at -20 °C until further use.

Material characterization.

(a) Morphology and structure characterization: A scanning electron microscope (SEM, TESCAN, VEGA3, Czech Republic) was utilized to visualize the morphology and structure of 2D NMs and 3D NSs. Before SEM observation, the samples were sprayed with gold for 60 s to increase the electrical conductivity. An accelerated high voltage of 10 kV was adopted for image taking. ImageJ software (NIH, USA) was employed to analyse the average

fibre diameter. The calculation for each specimen randomly selected more than 100 different locations from 3 different SEM images. The expansion height of different 3D NSs was measured by using a Vernier caliper. Five independent replicates were recorded, and the average value was analysed.

(b) FTIR test: A Fourier transform infrared spectrometer (Thermo Fisher, Nicolet 8700, USA) was used to record the Fourier transform infrared (FTIR) curves of different 2D NMs and 3D NSs. The scanning range and resolution were set as 500-4000 cm^{-1} and 2 cm^{-1} , respectively.

(c) XRD test: The XRD diffraction patterns of different 2D NMs and 3D NSs were analysed using an X-ray diffractometer (Rigaku Ultima IV, Cu K α radiation, Japan). The tests were performed in the range of 5° to 60° at a speed of 5°/min.

(d) Tensile test: A universal mechanical tester (Instron 5965, USA) was used to measure the mechanical properties of different samples. The samples were clamped with a fixed gauge length of 10 mm with a preload force of 0.02 N applied. After being fixed, stretching was applied at a speed of 10 mm/min until fracture occurred. Five independent replicates of each group were conducted and analysed. The load-elongation curves were recorded, and the necessary mechanical parameters, including Young's modulus, ultimate strength, and ultimate strain, were statistically calculated.

NSC harvesting, culture, implantation, and differentiation.

NSCs were isolated from SD rats or *Gfp*⁺ transgenic SD rats (Cyagen, China). In brief, the rats at 13-15 days gestation were sacrificed. The cerebral cortex of embryos was dissected and dissociated into single-cell suspensions. The cell suspension was cultured in serum-free Dulbecco's modified Eagle's medium (DMEM)/F12 (1:1, Gibco, USA) supplemented with 2% B27 (Gibco, USA), 20 ng/mL basic fibroblast growth factor (bFGF, Peprotech, USA), and 20 ng/mL epidermal growth factor (EGF, Peprotech, USA). As time went on, the NSCs assembled into neurospheres in the suspension, which were dissociated and passaged by Accutase (Gibco, USA) approximately once each week, with half of the medium replaced every 3 days.

After 7 days of culture, the neurospheres were centrifuged and further digested into single cells with Accutase. Single cells were seeded on sterilized 2D TCPS plates (ibidi, USA), and 3D PCL/PPDO NSs were both precoated with 10 µg/mL poly-L-lysine (Sigma, USA). The seeded cells were cultured in DMEM/F12 (1:1) with 2% B27 and 10% foetal bovine serum (FBS, Gibco, USA). After 4 hours, the medium was replaced with differentiation medium consisting of DMEM/F12 (1:1) with 2% B27 and 1% FBS to identify the differentiation potential of NSCs.

Viability and proliferation characterizations of NSCs.

To visually monitor the survival state of NSCs, live/dead staining was

performed by adding calcein-AM (1:1000, Beyotime, China) and propidium iodide (PI, 1:1000, Beyotime, China) to the culture medium at 37 °C for 30 min. The cells were washed three times with PBS and visualized using an ultra-high-resolution confocal fluorescence microscope (Leica DMI8, Germany). Cell proliferation was detected by using a CCK-8 (Dojindo, Japan) throughout 7 days of culture. On days 1, 3, and 7, the CCK-8 assay was performed according to the manufacturer's protocol. The absorbance value at 450 nm was examined with a microplate reader (PerkinElmer EnSight, USA).

Surgery and scaffold transplantation.

Adult female SD rats (220–250 g) were purchased from SPF Biotechnology (China), and the animal experiments were approved by the Animal Care and Experiment Committee of Qilu Hospital affiliated with Shandong University (approval No.: DWLL-2021-005) and carried out following the local animal care guidelines.

A total of 40 rats were randomly divided into 4 groups, namely, the Sham group, SCI group (no treatment after SCI), 3D NS group (transplantation of 3D NSs after SCI), and 3D NS + NSC group (transplantation of NSCs-loaded 3D NSs after SCI). During surgery, isoflurane was used for gas anaesthesia. Following laminectomy, the T10 spinal cord was hemisected, and a 3 mm cord segment was removed. After haemostasis was achieved, 3D NSs were transplanted

into the lesion gap, followed by incision closure. After the operation, all rats routinely received ceftiofur sodium (Amicogen, China) for 7 days. The bladder was manually massaged twice a day until the bladder restored automatic urination. Cyclosporine A (Selleck, USA) was intraperitoneally (i.p.) administered at a dose of 10 mg/kg/d until the rats were sacrificed.

IF staining.

Samples were fixed with 4% paraformaldehyde for 15 min and incubated in 0.3% Triton X-100 for 15 min at room temperature. After blocking with 5% bovine serum albumin (BSA, ZSGB Bio, China) for 1 hour, the samples were incubated with primary antibodies at 4 °C overnight and then incubated with Alexa Fluor 488-conjugated or Alexa Fluor 594-conjugated secondary antibodies (ZSGB Bio, China) for 1 h and DAPI (Beyotime, China) for 15 min at room temperature. The staining results were photographed by an ultra-high-resolution confocal fluorescence microscope (Leica DMI8, Germany) or a panoramic digital section scanning microscope (OLYMPUS VS120, Japan). The semi-quantitative fluorescence analysis was carried out with ImageJ software. The following primary antibodies were used: mouse anti-Nestin (1:1000, ab6142, Abcam, UK); mouse anti-Tuj-1 (1:1000, ab78078, Abcam, UK); mouse anti-NeuN (1:1000, ab104224, Abcam, UK); mouse anti-NF200 (1:600, 2836, CST, USA); rabbit anti-DCX (1:1000, ab18723, Abcam, UK); rabbit anti-GFAP (1:1000, 12389, CST, USA); rabbit anti-ChA

(1:200, ab181023, Abcam, UK); rabbit anti-5-HT (1:5000, S5545, Solarbio, China); and rabbit anti-Syn (1:200, 5297, CST, USA).

Locomotor function assessments.

The open-field test and other tests were carried out to evaluate the motor functional recovery of rats following SCI (n=6). BBB scoring was performed in the open field on 0, 1, 3, 7, 14, 21, 28, 35, 42, 49, and 56 days post-injury (dpi) to semi-quantitatively analyse the voluntary movements of hindlimbs. The scores were calculated ranging from 0 (complete paralysis) to 21 (normal locomotion).

An inclined plane test was used to evaluate the animals' grip at 4, 6, and 8 weeks post-injury. The rats were placed on the inclined plate with a rubber pad, and the longitudinal axis of the rat was kept parallel to the longitudinal axis of the inclined plate. The height of the inclined plate was slowly raised to the maximum angle, where the rat could stay on the inclined plate for 5 s. Each rat was measured 5 times, and the average value was taken.

For the footprint analysis, animals were first trained to walk on the runway (60 cm×10 cm). On the test day (4, 6, and 8 wpi), the forepaws and hindpaws of animals were stained with red ink and blue ink, respectively. Then, they were placed onto the same runway covered with white paper to track the footprints.

The rotation angle was defined as the angle of the hindpaw axis (injured side) relative to the runway axis. The interlimb coordination was represented by the relative position between the forepaws and hindpaws.

Sensory function assessment.

The adhesive removal test is a sensitive method to assess sensory deficits and recovery³⁴. At 8 wpi, each animal was put into individual clear containers without any bedding for at least 5 min. After that, a piece of tape (15×15 mm) was stuck on the palm of the hindpaw (injured side). The time that animals sensed the tape was recorded to indicate sensory function recovery after SCI.

MR imaging evaluation.

MRI experiments were carried out on a 3.0 Tesla MR scanner (Siemens, MAGNETOM Verio 3.0, Germany) with a wrist coil at 4 wpi. Under anaesthesia, sagittal T2-weighted turbo spin-echo images (T2WI) of thoracic vertebra were acquired with the following parameters: repetition time (TR)= 3610 ms; echo time (TE)= 74 ms; slice thickness= 1.0 mm; field of view (FOV)= 120 mm×120 mm; average= 3.

Electrophysiological analysis.

At 8 wpi, electrophysiological examinations were performed to evaluate the functional status of sensorimotor signal conduction as previously described².

Briefly, under anaesthesia, the sciatic nerve and sensorimotor cortex (SMC) of the animals were exposed. To record the MEPs, the stimulating electrode was inserted into the SMC, while the recording electrode was inserted into the sciatic nerve. The stimulus voltage was 42 V, and the pulse width was 0.2 ms. Conversely, the stimulating electrode was inserted into the sciatic nerve while the recording electrode was inserted into the SMC to record SEPs. The stimulus current was 32 mA. Then, the waveforms, amplitude, and latency of MEP and SEP were acquired and analysed.

RNA sequencing and bioinformatics analysis.

TRIzol reagent was used to extract total RNA from NSCs cultured on the 2D TCPS plates control and 3D NSs at day 7 (n=3). Total RNA was isolated employing the RNeasy mini kit (Qiagen, Germany), and RNA-Seq libraries were prepared using the Illumina TruSeq RNA sample preparation kit (Illumina, USA) and sequenced through paired-end (150 base paired-end reads) sequencing on the Illumina NovaSeq. 6000 platform. Raw data were then quality filtered to generate “clean reads” for further analysis. The differentially expressed genes (P value ≤ 0.05 , $|\text{Log}_2\text{FC}| \geq 1$) were subjected to enrichment analysis of GO and KEGG pathways using Hiplot (<https://hiplot.com.cn>).

Statistical analysis.

Statistical analysis was performed with GraphPad Prism software (version 7.0).

Data are presented as the mean \pm standard deviation (S.D.). All experiments were performed with at least 3 replicates in each group. Unpaired Student's t test (two-tailed) was used for the mean comparison of two groups. One-way ANOVA followed by Tukey's post hoc analysis was used to compare the mean values of three groups and more. Data were analysed by two-way ANOVA in the BBB scores matched at different time points. $P < 0.05$ was determined to be statistically significant.

Data availability.

All data is available from the authors upon reasonable request.

Reference

- 1 Rubiano, A. M., Carney, N., Chesnut, R. & Puyana, J. C. Global neurotrauma research challenges and opportunities. *Nature* **527**, S193-197 (2015).
- 2 Koffler, J. *et al.* Biomimetic 3D-printed scaffolds for spinal cord injury repair. *Nat Med* **25**, 263-269 (2019).
- 3 Courtine, G. & Sofroniew, M. V. Spinal cord repair: advances in biology and technology. *Nat Med* **25**, 898-908 (2019).
- 4 George, J., Hsu, C. C., Nguyen, L. T. B., Ye, H. & Cui, Z. Neural tissue engineering with structured hydrogels in CNS models and therapies. *Biotechnol Adv* **42**, 107370 (2020).
- 5 Ong, W., Pinese, C. & Chew, S. Y. Scaffold-mediated sequential drug/gene delivery to promote nerve regeneration and remyelination following traumatic nerve injuries. *Adv Drug Deliv Rev* **149-150**, 19-48 (2019).
- 6 Chen, S., Li, R., Li, X. & Xie, J. Electrospinning: An enabling nanotechnology platform for drug delivery and regenerative medicine. *Adv Drug Deliv Rev* **132**, 188-213 (2018).
- 7 Ding, Y. *et al.* Electrospun Fibrous Architectures for Drug Delivery, Tissue Engineering and Cancer Therapy. *Advanced Functional Materials* **29**, 1802852 (2019).
- 8 Taskin, M. B. *et al.* Bioactive Electrospun Fibers: Fabrication Strategies and a Critical Review of Surface-Sensitive Characterization and Quantification. *Chem Rev* **121**, 11194-11237 (2021).
- 9 Xue, J., Pisignano, D. & Xia, Y. Maneuvering the Migration and Differentiation of Stem Cells with Electrospun Nanofibers. *Adv Sci (Weinh)* **7**, 2000735 (2020).

737 10 Assinck, P., Duncan, G. J., Hilton, B. J., Plemel, J. R. & Tetzlaff, W. Cell transplantation
738 therapy for spinal cord injury. *Nat Neurosci* **20**, 637–647 (2017).

739 11 Xi, K. *et al.* Microenvironment-responsive immunoregulatory electrospun fibers for
740 promoting nerve function recovery. *Nat Commun* **11**, 4504 (2020).

741 12 Xue, W., Shi, W., Kong, Y., Kuss, M. & Duan, B. Anisotropic scaffolds for peripheral nerve
742 and spinal cord regeneration. *Bioact Mater* **6**, 4141–4160 (2021).

743 13 Jiang, J. *et al.* Expanded 3D Nanofiber Scaffolds: Cell Penetration, Neovascularization,
744 and Host Response. *Adv Healthc Mater* **5**, 2993–3003 (2016).

745 14 Chen, S. *et al.* Three-Dimensional Objects Consisting of Hierarchically Assembled
746 Nanofibers with Controlled Alignments for Regenerative Medicine. *Nano Lett* **19**,
747 2059–2065 (2019).

748 15 Yang, L. *et al.* A biodegradable hybrid inorganic nanoscaffold for advanced stem cell
749 therapy. *Nat Commun* **9**, 3147 (2018).

750 16 Stenudd, M., Sabelström, H. & Frisé, J. Role of endogenous neural stem cells in spinal
751 cord injury and repair. *JAMA Neurol* **72**, 235–237 (2015).

752 17 Sabelström, H. *et al.* Resident neural stem cells restrict tissue damage and neuronal loss
753 after spinal cord injury in mice. *Science* **342**, 637–640 (2013).

754 18 Tai, W. *et al.* In vivo reprogramming of NG2 glia enables adult neurogenesis and
755 functional recovery following spinal cord injury. *Cell Stem Cell* **28** (2021).

756 19 Li, X. *et al.* A collagen microchannel scaffold carrying paclitaxel-liposomes induces
757 neuronal differentiation of neural stem cells through Wnt/ β -catenin signaling for spinal
758 cord injury repair. *Biomaterials* **183**, 114–127 (2018).

759 20 Lee, Y. *et al.* Oligodendroglia metabolically support axons and contribute to
760 neurodegeneration. *Nature* **487**, 443–448 (2012).

761 21 Cohen, S., Nathan, J. A. & Goldberg, A. L. Muscle wasting in disease: molecular
762 mechanisms and promising therapies. *Nat Rev Drug Discov* **14**, 58–74 (2015).

763 22 Joung, D. *et al.* 3D Printed Stem-Cell Derived Neural Progenitors Generate Spinal Cord
764 Scaffolds. *Adv Funct Mater* **28** (2018).

765 23 Chen, S., Li, R., Li, X. & Xie, J. Electrospinning: An enabling nanotechnology platform for
766 drug delivery and regenerative medicine. *Adv Drug Deliv Rev* **132**, 188–213 (2018).

767 24 Zhang, N. *et al.* A 3D Fiber-Hydrogel Based Non-Viral Gene Delivery Platform Reveals
768 that microRNAs Promote Axon Regeneration and Enhance Functional Recovery
769 Following Spinal Cord Injury. *Adv Sci (Weinh)* **8**, e2100805 (2021).

770 25 Puhl, D. L., Mohanraj, D., Nelson, D. W. & Gilbert, R. J. Designing electrospun fiber
771 platforms for efficient delivery of genetic material and genome editing tools. *Adv Drug*
772 *Deliv Rev* **183**, 114161 (2022).

773 26 Pawelec, K. M. *et al.* Microstructure and in vivo characterization of multi-channel nerve
774 guidance scaffolds. *Biomed Mater* **13**, 044104 (2018).

775 27 Dalton, P. D., Flynn, L. & Shoichet, M. S. Manufacture of poly(2-hydroxyethyl
776 methacrylate-co-methyl methacrylate) hydrogel tubes for use as nerve guidance
777 channels. *Biomaterials* **23**, 3843–3851 (2002).

778 28 Hung, T. K., Chang, G. L., Lin, H. S., Walter, F. R. & Bunegin, L. Stress-Strain Relationship
779 of the Spinal-Cord of Anesthetized Cats. *J Biomech* **14**, 269–276 (1981).

780 29 Zhou, L. *et al.* Soft Conducting Polymer Hydrogels Cross-Linked and Doped by Tannic

- 781 Acid for Spinal Cord Injury Repair. *ACS Nano* **12**, 10957-10967 (2018).
782 30 Kadoya, K. *et al.* Spinal cord reconstitution with homologous neural grafts enables robust
783 corticospinal regeneration. *Nature medicine* **22**, 479-487 (2016).
784 31 Kong, Y. *et al.* Regulation of stem cell fate using nanostructure-mediated physical signals.
785 *Chem Soc Rev* **50**, 12828-12872 (2021).
786 32 Hao, M. *et al.* Hydroxyapatite Nanorods Function as Safe and Effective Growth Factors
787 Regulating Neural Differentiation and Neuron Development. *Advanced Materials* **33**,
788 2100895 (2021).
789 33 Xu, Y. *et al.* Understanding the role of tissue-specific decellularized spinal cord matrix
790 hydrogel for neural stem/progenitor cell microenvironment reconstruction and spinal
791 cord injury. *Biomaterials* **268**, 120596 (2021).
792 34 Han, Q. *et al.* Restoring Cellular Energetics Promotes Axonal Regeneration and
793 Functional Recovery after Spinal Cord Injury. *Cell Metab* **31**, 623-641.e628 (2020).

794

795 **Competing Interests statement**

796 The authors declare no competing interests.

797

Figure 1

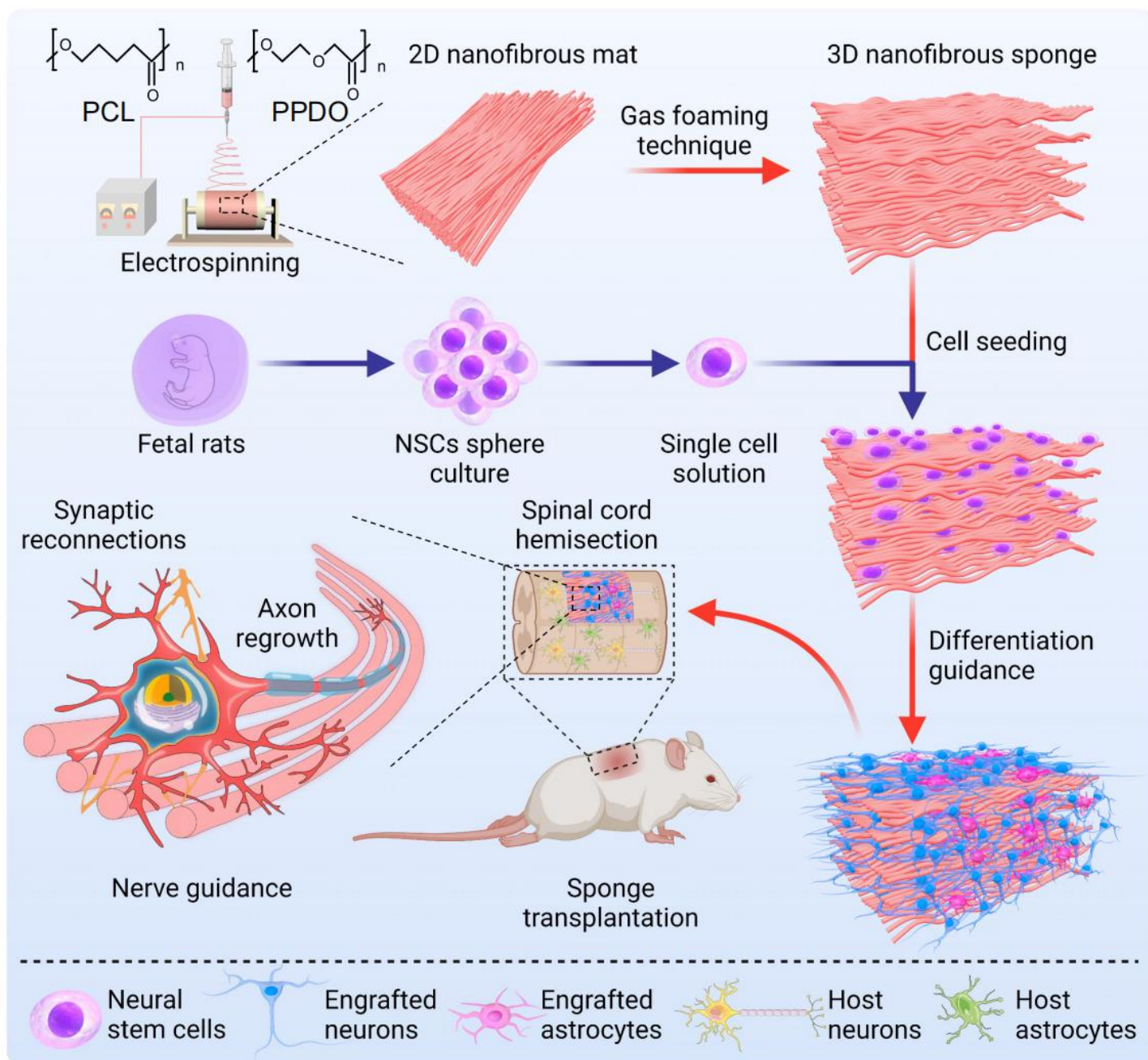


Figure 1. Illustration of the fabrication of 3D NSs and the application of NSC-seeded 3D NSs for SCI treatment. A directional electrospinning method was performed to fabricate aligned 2D PCL/PPDO NMs, which were subsequently expanded into 3D PCL/PPDO NSs through a gas-foaming technique. Exogenous NSCs harvested from foetal rats were seeded on the as-obtained 3D NSs, and the 3D NSs could effectively regulate the fate of NSCs. Eventually, the NSC-NS constructs were implanted into the lesion gap to bridge nerve stumps in hemisected SCI rat models.

Figure 2

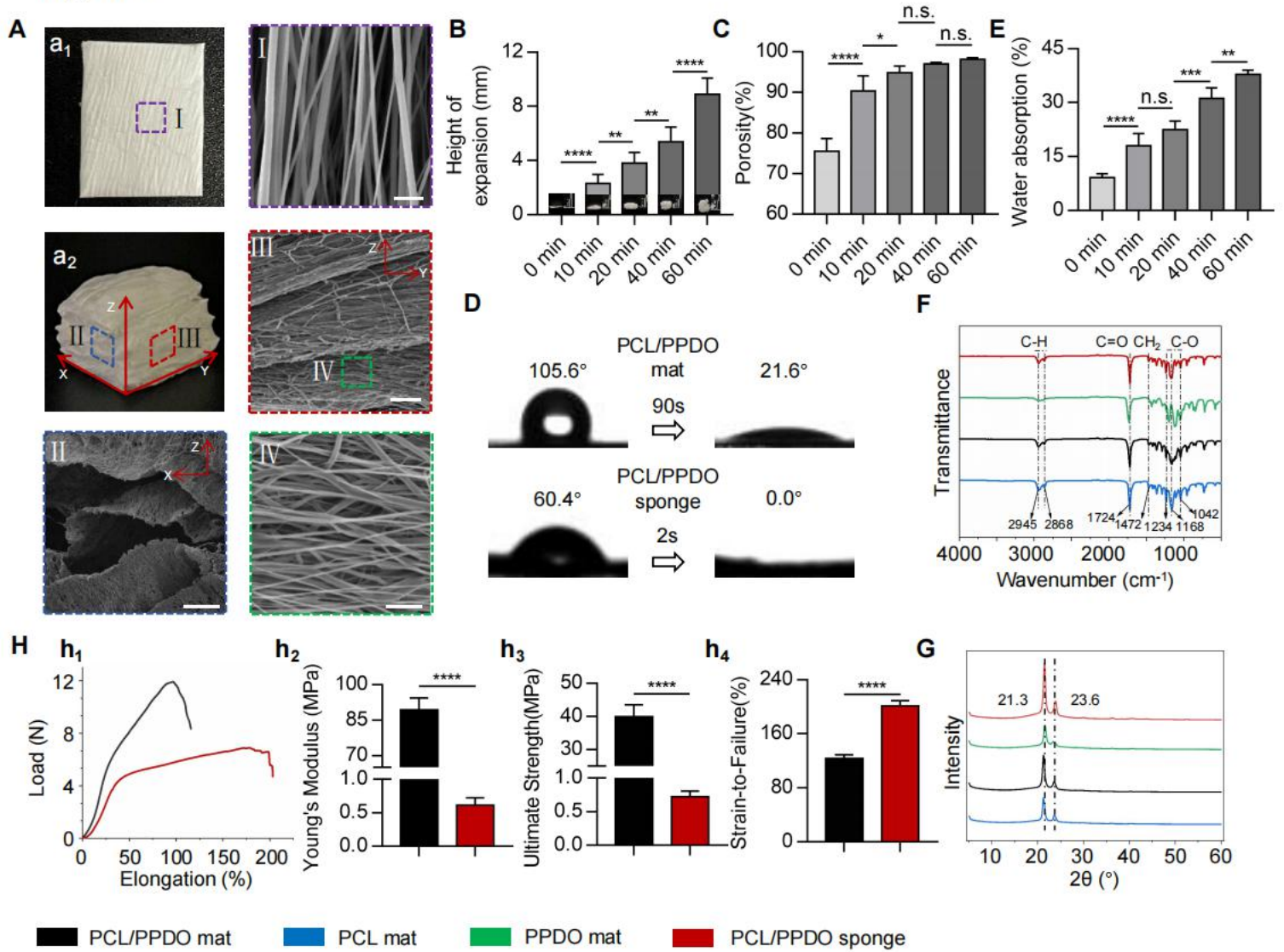


Figure 2. Characterization of 2D NMs and 3D NSs. (A) Digital photographs and SEM images of 2D NMs (a1, I) and 3D NSs (a2, II-IV). Scale bars were 5 μm , 100 μm , 25 μm , and 10 μm for images I-IV, respectively. Statistical analysis of the expansion height (B), porosity (C), and water absorption (E) of 3D NSs generated from different gas-forming times ($n=10$). (D) Water contact angle of 2D PCL/PPDO NMs and 3D PCL/PPDO NSs. (F) Uniaxial mechanical testing of scaffolds ($n=5$): (f1) Representative load-elongation curves; (f2) Young's modulus; (f3) Ultimate strength; (f4) Strain-to-failure; (G) FTIR spectra and (H) XRD patterns of 2D PCL NMs, PPDO NMs, 2D PCL/PPDO NMs, and

815 3D PCL/PPDO NSs. * $P < 0.05$, ** $P < 0.01$, *** $P < 0.001$, and **** $P < 0.0001$

816 indicate significant differences.

Figure 3

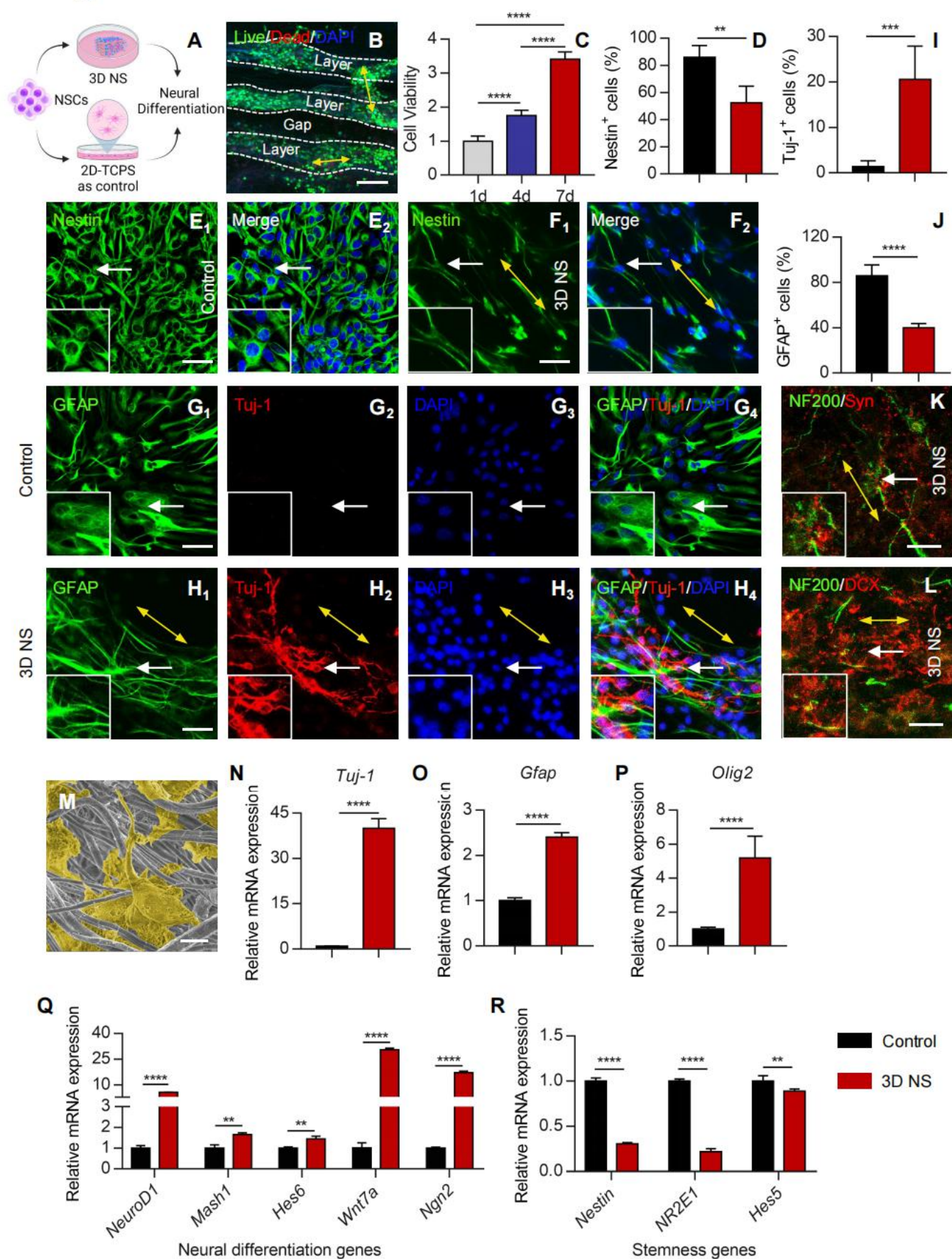


Figure 3. 3D NSs enhanced the survival, neuronal differentiation, and

maturation of NSCs. (A) Schematic illustration of NSCs cultured on 2D TCPS plates or 3D PCL/PPDO NSs for further experiments. (B) Live (green)/dead (red) cellular staining of NSCs seeded and cultured on 3D NSs in the lateral view at day 7 (scale bar = 75 μ m). Nuclei were counterstained with DAPI (blue). (C) Cell viability of NSCs cultured on 3D NSs at days 1, 3, and 7 (n = 4). **** $P < 0.0001$. (D) Percentage of Nestin⁺ cells (green) in the 2D TCPS plate control group (E, n = 4) and 3D NS group (F, n = 5) based on the corresponding IF staining (scale bar = 50 μ m). The yellow bidirectional arrows indicate the direction of cell extension. Enlarged views of the regions indicated with white arrows are shown in the lower left corner ** $P < 0.01$). (G, H) Representative IF staining images of Tuj-1 (red) and GFAP (green) in NSCs in the 2D TCPS plate control group and 3D NS group at day 7 (scale bar = 50 μ m). (I, J) Statistical analysis of the percentage of Tuj-1⁺ cells (n=5) and GFAP⁺ cells (n=5). *** $P < 0.001$ and **** $P < 0.0001$). Representative IF staining images of NF200 (green)/Syn (red) (K) and NF200 (green)/DCX (red) (L) in the 3D NS group at day 7 (scale bar = 20 μ m). (M) Representative SEM images of NSCs seeded and cultured on 3D NSs at day 7. The cells are highlighted with yellow pseudo-colour (scale bar = 3 μ m). Relative mRNA expression of *Tuj-1* (N), *Gfap* (O), *Olig2* (P), neural differentiation-related genes (Q), and stemness-related genes (R) in the 2D TCPS plate control group (n = 3) and 3D NS group (n = 3) via RT-qPCR. ** $P < 0.01$ and **** $P < 0.0001$ indicate significant differences.

Figure 4

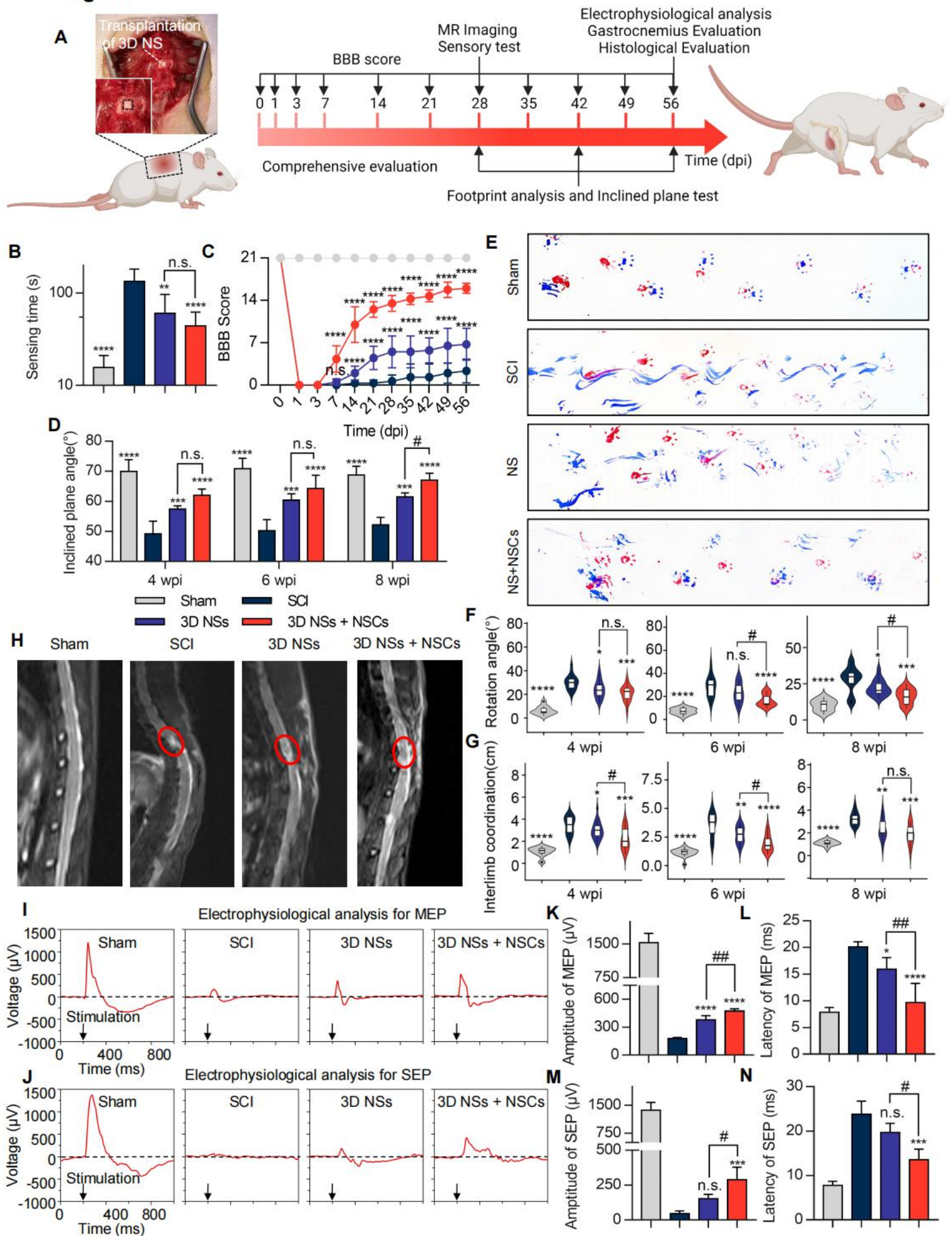


Figure 4. Transplantation of NSCs-seeded 3D NSs significantly promoted neurological functional recovery in SCI rats. (A) Schematic illustration of the animal experiment and timeline. (B) Sensing time of Sham, SCI, 3D NSs, and 3D NS + NSC groups by using adhesive removal test at 4 wpi (n = 5, ** P<0.01 and **** P<0.0001 when SCI compared with other groups). (C) Evaluation of locomotor functional recovery by BBB score throughout 56 days of treatment (n = 6). (D) Inclined plane test in the Sham (n=6), SCI (n = 5), 3D NS (n = 5), and 3D NS + NSC (n = 5) groups at 4, 6, and 8 wpi. (E) Representative footprints with the forelimbs (red) and hindlimbs (blue) and the corresponding semi-quantitative analysis of (F) rotation angle and (G) interlimb coordination at 4, 6, and 8 wpi (n=10). Statistical analysis of the BBB score, inclined plane tests, and footprint analysis was performed at the same time point (*, **, ***, and **** indicate P<0.05, P<0.01, P<0.001, and P<0.0001, respectively, when SCI was compared with the other groups, and # indicates p<0.05 when the 3D NS group was compared with the 3D NS + NSC group). (H) Typical MR imaging data in T2WI at 4 wpi. Electrophysiological signals of (I) MEP and (J) SEP at 8 wpi. The dark arrows represent the time point of electrical stimulation. The amplitude and latency of (K, L) MEP (n = 4) and (M, N) SEP (n = 3) were quantified. * P<0.05, *** P<0.001, and **** P<0.0001 when comparing the SCI and other groups. # P<0.05 and ## P<0.01 when comparing the 3D NSs and 3D NS + NSC groups.

Figure 5

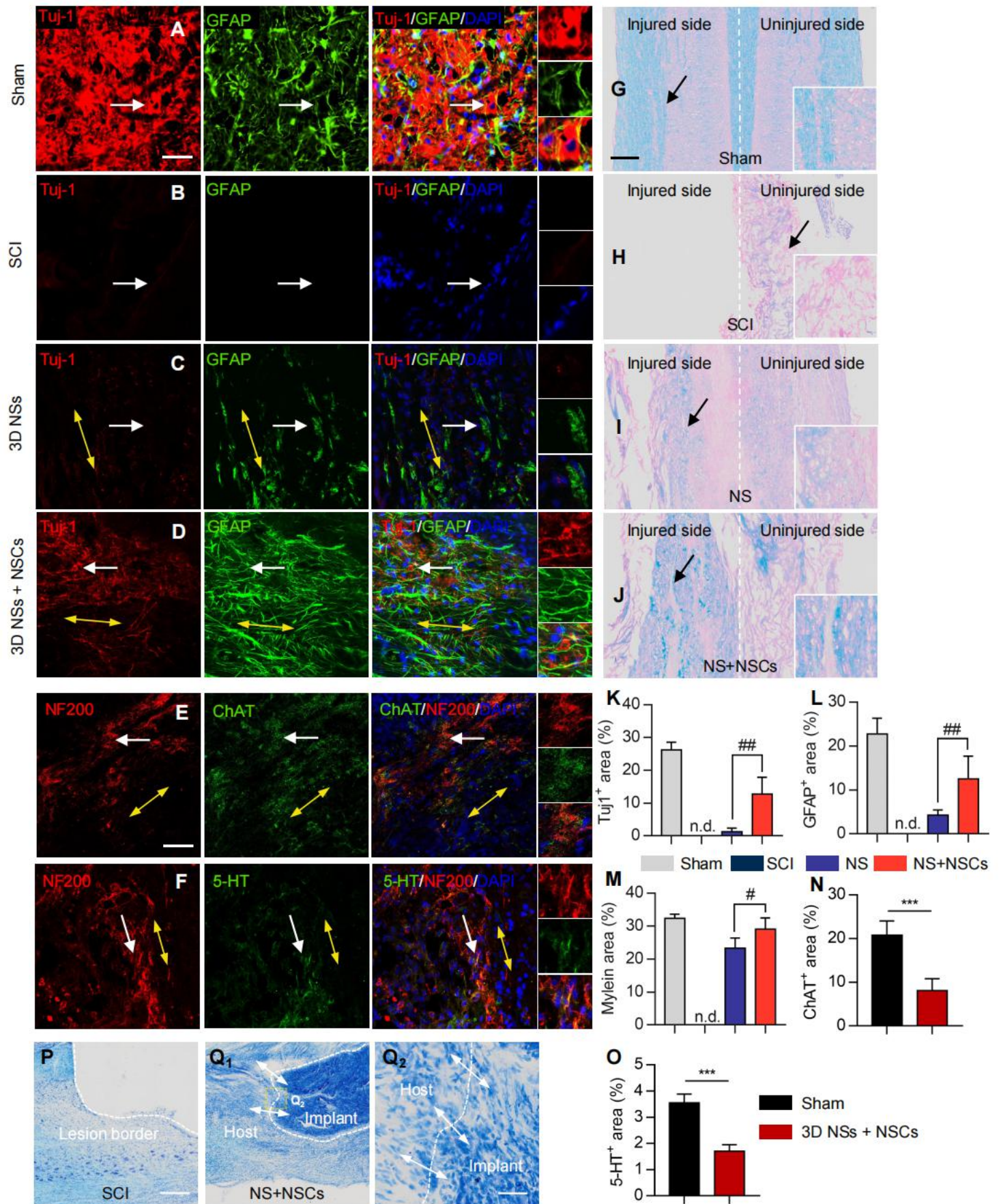


Figure 5. Histological evaluation of regenerated spinal cord tissues by using NSC-seeded 3D NSs during the chronic SCI stage. Representative IF staining images of Tuj-1 (red) and GFAP (green) in the (A) Sham, (B) SCI, (C) 3D NS, and 3D NS + NSC (D) groups (scale bar = 50 μ m) at 8 wpi. Nuclei were counterstained with DAPI (blue). The yellow bidirectional arrows represent the contact guiding effect of oriented nanofibres on neurofilaments. Enlarged views of the regions indicated with white arrows are shown in the right panels. Representative IF staining images of (E) NF200 (red)/ChAT (green) and (F) NF200 (red)/5-HT (green) in the 3D NS + NSC group at 8 wpi (scale bar = 50 μ m). Representative LFB staining images in the (E) Sham, (F) SCI, (G) 3D NS, and (H) 3D NS + NSC groups (scale bar = 300 μ m). Semi-quantification of the area ratio of (K) Tuj-1⁺ (n = 5), (L) GFAP⁺ (n = 5), (M) myelin sheath (n = 4), (N) ChAT⁺ (n = 4), and (O) 5-HT⁺ (n = 4) at the lesion epicentre. # P<0.05 and ## P<0.01 when comparing the 3D NS group and the 3D NS + NSC group. *** P<0.001 when comparing the Sham group and the 3D NS + NSC group. (P, Q) Representative Nissl staining images in the (P) SCI group and (Q₁, Q₂) 3D NS + NSC group at 8 wpi (scale bar = 500 μ m). An enlarged view of the box region is shown in Q₂ (scale bar = 50 μ m). The white dashed line and white bidirectional arrows represent the lesion border and cell infiltration, respectively.

A

[illegible]

- C**

Figure 2 is a chord diagram illustrating the distribution of 100 genes across 10 cell types. The genes are listed on the left and right sides of the diagram, and the cell types are listed at the bottom. The thickness of the lines (chords) represents the number of genes shared between the cell types. A legend on the right indicates the size of the dots: 10, 20, 30, and 40.

Genes listed on the left (clockwise from top): Ush2a, Mapk15, Grm4, Rpn11, Ckap69, Rprg, Fam161b, Ctn3, Eno1, Intu1, Igcc, Ckap100, RspHr, Drc1, CenAlms1, Cep290, Tcte1, Tpb1, Agbl2, Cibar2, Bbo1, Ckap126, CrocMlf1, Ttc29, Pife, Cacna1c, Capdh, Saxo2, Eno6, Grin2b, Rkar1b, Spata18, Mx1, Ptpz1, Ccdc4, Dnah1, Ttr, Cald1, Dnah1, Dnah9, Penk, Adora1, Slc26g5, Sstm1, Glra2, Paccin1, Scn8a, Dync2h1, Aldoa, Glra1, Adam22, LOC10369, Spag17, Lca5l, Shank3, Shank1, Ccdc10, Dnaaf1, Erbpb, Stxbp5, Traf3ip1, Slc16a3, Bnip3, LOC100364, Kif19, Slc8a3, Mx2, LOC100359, Rns4x1, Hydin, Shank2, Peb1, LOC100359, Dnah7, Grin3a, Eps8, Rpl11, Cenpf, Egin1, Lrrc4c, Rpl27a, Rpl12, Rpl3.

Cell types listed at the bottom (clockwise from top): 10, 20, 30, 40.

- F**

[illegible]

D

F

Enrichment score

Count

$-\log_{10}(\text{P Value})$

Figure 6. Potential differentiation mechanisms of NSCs seeded and cultured on 3D NSs using mRNA sequencing. (A) Gene-concept network and (B) GO concept network and (D) GO enrichment map of cellular components via GO analysis. (E) Top 20 KEGG pathway analyses. Red dashed circles indicate the related processes, components, and pathways related to neural differentiation and neurogenesis. (F) Schematic illustration of the potential mechanisms of enhanced neurogenesis when NSCs were seeded and cultured on 3D NSs.

Supplementary Files

This is a list of supplementary files associated with this preprint. Click to download.

- [Supportinginformation20220326naturecommunications.pdf](#)
- [expansion.mp4](#)
- [watercontact.mp4](#)
- [compression.mp4](#)
- [BBBvideo.mp4](#)